Transition between advection and inertial wave propagation in rotating turbulence

Jonathan A. Brons[1,2,†], **P. J. Thomas**[1] **and A. Pothérat**[2]

[1]Fluid Dynamics Research Centre, School of Engineering, University of Warwick, Coventry CV4 7AL, UK

[2]Fluid and Complex Systems Research Centre, Coventry University, Coventry CV1 5FB, UK

In turbulent flows subject to strong background rotation, the advective mechanisms of turbulence are superseded by the propagation of inertial waves, as the effects of rotation become dominant. While this mechanism has been identified experimentally (Dickinson & Long, *J. Fluid Mech.*, vol. 126, 1983, pp. 315–333; Davidson, Staplehurst & Dalziel, *J. Fluid Mech.*, vol. 557, 2006, pp. 135–144; Staplehurst, Davidson & Dalziel, *J. Fluid Mech.*, vol. 598, 2008, pp. 81–105; Kolvin *et al. Phys. Rev. Lett.*, vol. 102, 2009, 014503), the conditions of the transition between the two mechanisms are less clear. We tackle this question experimentally by tracking the turbulent front away from a solid wall where jets enter an otherwise quiescent fluid. Without background rotation, this apparatus generates a turbulent front whose displacement recovers the $z(t) \sim t^{1/2}$ law classically obtained with an oscillating grid (Dickinson & Long, *Phys. Fluids*, vol. 21 (10), 1978, pp. 1698–1701) and we further establish the scale independence of the associated transport mechanism. When the apparatus is rotating at a constant velocity perpendicular to the wall where fluid is injected, not only does the turbulent front become mainly transported by inertial waves, but advection itself is suppressed because of the local deficit of momentum incurred by the propagation of these waves. Scale-by-scale analysis of the displacement of the turbulent front reveals that the transition between advection and propagation is local both in space and spectrally, and takes place when the Rossby number based on the considered scale is of order unity, or equivalently, when the scale-dependent group velocity of inertial waves matched the local advection velocity.

Key words: rotating flows, waves in rotating fluids, rotating turbulence

1. Introduction

The main transport mechanism in turbulent flow is advection. When turbulent flows are subject to background rotation, however, inertial waves offer an additional transport mechanism. The competition between them determines the anisotropy and transport properties of rotating turbulence. Here, we determine the conditions in which either of them dominates, and especially the scale dependence of this competition.

Turbulence in rotation arises in a variety of industrial and natural contexts, such as centrifuges, precessing spacecraft or oceanographic and atmospheric flows (Vanyo 1993; Davidson 2013, 2015), where its specific transport and dissipative properties

† Email address for correspondence: ac2002@coventry.ac.uk

influence or even govern the dynamics of the processes involved. Its most distinctive feature is to form large, more or less, columnar structures aligned with the rotation axis that are perhaps most conspicuous in geophysical flows (Pedlosky 1987). The emergence of columnar structures in rotating flow was first reported in a letter by Kelvin (Thomson 1868) and subsequently illustrated in Taylor's famous experiment (Taylor 1922). Since then, a number of experiments and numerical simulations have reported the emergence of such columns in turbulent flows (Hopfinger, Browand & Gagne 1982; Bartello, Métais & Lesieur 1994; Gallet 2015) and several scenarii have been proposed to explain their appearance. Underlying the question of how large columnar structures emerge, is that of the processes by which rotating flows and rotating turbulence transport momentum and energy. This question itself hinges on the role played by two essential ingredients of rotating turbulence. The first one is the propagation mechanism associated with linear inertial waves (see Greenspan (1968) for the theory of these waves): for a wavevector $\boldsymbol{k}$, with frequency ω and background rotation $\boldsymbol{\Omega}$, inertial waves follow the dispersion relation, and associated group velocity

$$\omega = \pm 2\boldsymbol{\Omega} \cdot \boldsymbol{e}_k, \quad \boldsymbol{v}_g = \pm \frac{2}{k}\boldsymbol{e}_k \times (\boldsymbol{\Omega} \times \boldsymbol{e}_k), \quad (1.1a,b)$$

where $\boldsymbol{e}_k = \frac{1}{k}\boldsymbol{k}$. The preferential transport of momentum along the rotation axis by inertial waves indeed elongates an initially isotropic blob of vorticity along the axis of rotation at a speed of Ωt (Davidson, Staplehurst & Dalziel 2006), where Ω is the rotation speed. The second ingredient involves nonlinear interactions (Cambon, Mansour & Godeferd 1997; Smith & Waleffe 1999; Cambon & Scott 1999). In this process, triadic interactions feed an inverse energy cascade towards large scales while non-resonant triads or quartets of waves transfer energy to modes aligned with the axis of rotation. This scenario is supported by numerical simulations and by strong experimental and numerical evidence of an inverse energy cascade (Campagne *et al.* 2014). However, Taylor's early experiments in a steady, laminar flow still exhibit anisotropic transport of momentum along the rotation in the absence of waves and nonlinearities. This waveless and linear anisotropic transport was indeed recovered in the analytical work of Moore & Saffman (1968, 1969) and Pothérat (2012), and suggests that more than a single transport mechanism may exist in rotating flows. Along this line, our recent experiments showed that even in turbulent flows, the anisotropy of the mean flow may not necessarily result from the action of inertial waves or triadic interactions (Brons, Thomas & Pothérat 2019). Instead, average anisotropy may emerge from an interplay between rotation and nonlinear advection, somewhat similar to the interplay between viscous diffusion and rotation in Taylor's laminar flow experiment. Advection and propagation of inertial waves were even found to simultaneously act on fluctuations in nearly two-dimensional flows: while larger scale fluctuations satisfied the dispersion relation for inertial waves, smaller scales behaved as inertial waves 'swept' by the surrounding velocity field of the large quasi-two-dimensional structures (Campagne *et al.* 2015).

With different mechanisms at play, the question arises of their precise respective domain of action, both in terms of the scales concerned and of the main control parameter, the Rossby number $Ro = U/2\Omega l$, that controls the ratio of inertial to Coriolis forces (U and l are typical velocity and length scale). One way to tackle the problem experimentally is to track the displacement of a turbulent front when the turbulence is produced by a localised forcing mechanism and progressively invades a domain of an otherwise quiescent fluid. Most experiments of this type involve either jets along the rotation axis or oscillating grids, as respectively pioneered by

McEwans (1976) and Dickinson & Long (1983). The latter showed that the position of the turbulent front evolved as $z_f \sim t^{1/2}$ as long as the local Rossby number based on z remained greater than unity. Past this point, Ro decreases, turbulence starts to exhibit wave patterns and the front travels as $z_f \sim \Omega t$, as consistent with the group velocity of inertial waves.

Grid experiments (Staplehurst, Davidson & Dalziel 2008) on the formation of columnar structures in rotating turbulence revealed that around a local critical Rossby number $Ro^{crit} \sim 0.4$ the flow transitions from a state where energy and momentum are mostly propagated by inertial waves (below Ro^{crit}) to one where they are mostly transported through advection. A recent numerical study on rotating turbulence ignited by a buoyancy anomaly showed that this transition could be spatially localised with some regions dominated by inertial waves, and others where they are absent (McDermott & Davidson 2019). These authors also confirmed a critical value of the Rossby number for this transition around 0.5, provided it is built on the correct large scale.

Recent scale-by-scale analysis of the turbulent front further showed that fluctuations were propagated at the group velocity of inertial waves corresponding to their length scales, in the limit of strong rotation $Ro \ll 1$ (Kolvin *et al.* (2009), turbulence initiated by jets). In statistically steady turbulence, jet experiments (Yarom & Sharon (2014), $0.006 \leqslant Ro \leqslant 0.2$), and experiments with a two-dimensional mechanical forcing (Campagne *et al.* 2015) confirmed that some of the fluctuations of frequency lower than 2Ω, the maximum frequency of inertial waves, satisfied the dispersion relation for inertial waves (but for the sweeping effect at high wavenumbers identified by Campagne *et al.* (2015)). The recent experiments of Burmann & Noir (2018) showed that inertial waves of a wide range of length scales emitted by a topography near an Ekman wall could speed up momentum transfer along the rotation axis and lead to an accelerated spin-up time following a step change in the rotation of a cylindrical vessel.

Although the role of inertial waves is clearly established in the limit $Ro \ll 1$ and in regions of the spectrum where $\omega \leqslant 2\Omega$, the limits of their regime of influence remains unclear, especially in terms of the length scales concerned. Both Dickinson & Long (1983) and Staplehurst *et al.* (2008) found that the momentum transport mechanism transitions from propagative regime to an advective one around Ro of the order of unity; however, the scale dependence of this transition remains unexplored. We set out to examine this question and, in particular, the scale dependence of the transport mechanisms in a transient turbulent flow under the effect of background rotation. We target regimes where rotation may not dominate over the entire turbulent spectrum. The specific questions we seek to answer are:

(i) Is there a clear scale separation (in terms of the control parameter and the scales concerned) between advective or nonlinear mechanisms on one side, and propagation on the other?

(ii) If so, what is the quantitative threshold defining such a separation?

Our approach relies on the tracking of the turbulent front in a flow forced by turbulent jets, with data processing techniques similar to those introduced by Kolvin *et al.* (2009) to analyse the scale dependence. The choice of a transient flow presents the advantage that momentum transport can be easily characterised by tracking the progression of the turbulent front. The experimental set-up is described in § 2. To characterise the phenomenology of pure advection in our experimental set-up, we first analyse non-rotating turbulence in the spirit of Dickinson & Long (1983) (§ 3), before running experiments at several rotational velocities (§ 4) and drawing conclusions (§ 5).
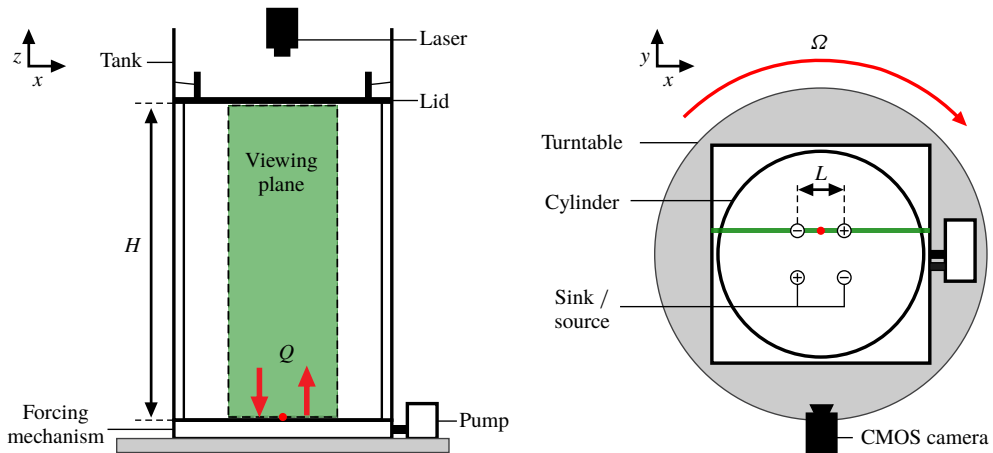
FIGURE 1. Sketch of the side and top view of the experimental set-up, highlighting all important components. The green rectangle shows the approximate size of the flow field recorded and the green line shows the position of the laser sheet across a source/sink pair. Red dots show the position of the origin in our experiments. In top view $(+)$ refers to a source and $(-)$ to a sink.

2. Experimental methods

2.1. *Experimental apparatus*

Figure 1 shows a sketch of the set-up. The experiment consists of a rectangular tank (60 cm $\times$ 32 cm $\times$ 32 cm) centred on a rotating turntable, filled with water (viscosity $\nu = 1.0034 \times 10^{-6}$ m^2 s^{-1} and density $\rho = 0.9982 \times 10^3$ kg m^{-3}). The temperature in the laboratory was kept at 20 °C.

A forcing mechanism, supported by four pillars at the corners of the mechanism, is placed underneath the bottom wall of the tank. This mechanism forces a flow by injecting and withdrawing fluid through four sources/sinks (diameter $d = 1$ mm) located at the corners of a square centred at the bottom wall of the tank. These sources and sinks are respectively identified by the $(+)$ and $(-)$ symbols in figure 1. The distance between the corners of the square is $L = 53$ mm. The choice of this square injection pattern provides a quadrupolar flow that remains near the centre of the vessel despite the wide range of Reynolds numbers we investigated. This ensures that measurements made in a fixed region of the flow but at different Reynolds numbers remain comparable to each other. The sources/sinks are connected to an external peristaltic pump via tubing housed underneath the forcing mechanism. The pump (Watson & Marlow 505-DI) is mounted on the turntable and allows for simultaneous fluid injection through one diagonal of the square (sources) and fluid withdrawal through the other diagonal (sinks), resulting in a zero net mass flux. The forcing mechanism is designed so that the difference in hydraulic resistance across each pair of sources/sinks is kept to a minimum, resulting in a difference in flow rates across these pairs of less than 0.1 %. The flow rate Q through each of the sources and sinks is considered constant with values of $(0.5, 0.9, 2.0, 3.1, 4.7, 9.4) \times 10^{-6}$ m^3 s^{-1}. A cylinder (height $H = 40$ cm, $\varnothing = 30$ cm) is placed inside the tank to provide support for a transparent lid placed atop, which prevents surface deformation and gives clear viewing window for the measurement system.

During experiments a Coriolis force is applied by spinning the rotating turntable at a constant rotation speed Ω. The turntable is driven by a DC-powered motor connected to the table via a belt drive; Ω spanned $\{0, 0.52, 1.04, 2.09, 4.19\}$ rad s^{-1} with an error on Ω below 1 %. The flow field is recorded using a two-dimensional particle image velocimetry (PIV) system. A laser sheet along the (x, z)-plane is aligned with a source–sink pair and illuminates an area of approximately 40 cm $\times$ 15 cm, covering the entire height of the tank, as can be seen in figure 1. The laser sheet is generated using a 1 W/532 nm diode laser and a custom lens system consisting of a concave, a convex and a cylindrical lens. The thickness of the laser sheet remains around 3 mm across the entire height of the flow field. The water is seeded with 10 μm silver-coated hollow glass spheres, used as tracer particles. Two 1.3MP CMOS cameras are used to record, respectively, the top and bottom halves of the flow field and cover an area of 21 cm $\times$ 15 cm each. The recorded areas of these cameras have a small overlapping region of approximately 1 cm at the centre height of the flow field. The cameras record at a frame rate of 60 f.p.s., that is sufficient to resolve the high velocities measured close to the point of fluid injection.

For each experimental run, the turntable is initially left to rotate until the fluid inside the tank has reached a state of solid body rotation with rotational velocity Ω. PIV data are then collected during approximately three seconds to measure the level of residual noise when the liquid is nominally at rest within the rotating frame of reference (i.e. in solid body rotation). Finally the forcing mechanism is activated, at time $t_0 = 0$, generating a set of jets which penetrate into the flow field. The flow field is recorded for a period of 3 min from the time of activation of the forcing mechanism. We identify a time t_{end} for which turbulence occupies the entire vessel. We found $t_{end} < 100$ s for all experiments. The injection system is then stopped and the flow is left to decay down to the level of noise recorded in solid body rotation, before the next activation of the injection system. Velocity fields are derived from recorded images by processing them using the PIVlab software (Thielicke & Stamhuis 2014) for Matlab. This is done on a 32×32 pixel grid with a 50 % overlap region. The combination of the camera resolution, its field of view and the resolution of the PIV grid result in the smallest resolvable length scale $\ell = 2.1$ mm. For each set of experimental parameters, a set of five separate measurements is recorded and the resultant velocity fields are averaged across these separate experiments in order to minimise uncertainties associated with the transient nature of the flow. This method is sufficient to capture the time-dependent event average of the velocity with a standard deviation of approximately 5 % across runs. Furthermore, although only the velocity components along the x and z directions are measured, the symmetry of the configuration implies that the flow is statistically invariant by a rotation of $\pm\pi/2$ followed by a reflection about a vertical plane equidistant from two electrodes. As such the two-dimensional (2-D) measurements provide a good representation of the three-dimensional dynamics, in particular for the purpose of estimating the group velocity of inertial waves of individual horizontal wavenumbers k.

2.2. *Control parameters*

We chose a rotating frame of reference with origin centred between two adjacent corners of the square, $\boldsymbol{e}_x$ and $\boldsymbol{e}_y$ in the horizontal plane and $\boldsymbol{e}_z$ pointing upwards, indicated by the red dot in figure 1.

Both Q and Ω provide control over two non-dimensional governing parameters, namely the Ekman number $Ek = \nu/2\Omega L^2 \in [17.0, 8.50, 4.25] \times 10^{-5}$ and a Reynolds

	Forcing	Re_Q	Ek	Ro_Q	z/L
Current	4 Jets	$(0.06–1.2) \times 10^4$	$(4.25–17.0) \times 10^{-5}$	0.026–2.04	0.1–7.4
Dickinson & Long (1983)[*]	Grid	n/a	$\geqslant 4.5 \times 10^{-6}$	n/a	120–187
Staplehurst et al. (2008)[*]	Grid	83–130	$(1.44–2.96) \times 10^{-6}$	0.5–1.4	120–187
Kolvin et al. (2009)[†]	248 Jets	$\leqslant 1300$	$(6.4–10.8) \times 10^{-6}$	$\leqslant 0.021$	1.4–11.4

TABLE 1. Comparison between the parameter range explored in the current experiment and experiments conducted in other studies. [*]Ekman numbers are based on the containers heights. [†]Based on Ω and upper bound for Q given by Kolvin et al.

number based on the flow rate, $Re_Q = U_0 d/\nu \in [600, 1200, 2500, 4000, 6000, 12\,000]$, where $U_0 = 4Q/\pi d^2$. Here L is chosen as the characteristic length scale to make comparison easier to previous experiments. Results are presented in non-dimensional form, using L and U_0 as reference length and velocity scales respectively. In comparison to the current experiment, Kolvin et al. (2009) applied a significantly stronger Coriolis force, while inertial forces were almost always weaker. This difference in parameters reflects a difference in purpose between both set-ups: while Kolvin et al.'s (2009) work targeted the limits of high rotation, and low inertia, we are targeting a transitional regime where inertia and the Coriolis force compete. Their ratio is measured by a Rossby number based on the injected velocity $Ro_Q = EkRe_Q$. For comparison with previous experiments on rotating turbulent fronts, the attainable values of the non-dimensional parameters are reported in table 1.

2.3. *Data analysis*

To differentiate advective from propagative processes, we shall analyse the scale dependence of the evolution of the turbulent front. For this, we follow a method similar to Kolvin et al. (2009): we first apply a discrete Fourier transform along x to the velocity field $\boldsymbol{u}(x, z, t)$ to obtain a space and time-dependent power density spectrum $E(k, z) = |\hat{\boldsymbol{u}}(k, z, t)^2|$, expressed in terms of wavenumber k. This operation is performed for each acquisition timestep t. From this, variations of energy at one spatial location for a given wavelength are extracted by fixing z and k.

Figure 2(a,b) shows example representations of $E(k, z, t)$ at $z/L = 4.91$ for one non-rotating and one rotating experiment, respectively. In each case, The time variations of $E(k, z, t)$ exhibit a sharp transition from an initially low energy state at noise level to a high energy, turbulent state. For any mode k, we consider that the front has arrived at height z at arrival time τ for the lowest value τ of t such that $E(k, z, t)$ exceeds a threshold value between these two states. For each set of parameters (Re_Q, Ek) and each value of k, the threshold value $E_T(k)$ is defined as $E_T(k) = ((1/2H)\int_0^H E(k, z, t_0)\,\mathrm{d}z) + ((1/2H)\int_0^H E(k, z, t_{end})\,\mathrm{d}z)$, i.e. the average between the state of residual noise at $t < t_0$, and the state when turbulence has invaded the full domain at $t = t_{end}$. The time of arrival at a prescribed height z of a given modes k is obtained as the time τ such that $E(k, z, \tau) = E_T(k)$. The position of the front at time τ of the physical domain containing energy in mode k is then simply tracked through the location $z(\tau)$ for which $E(k, z, \tau) = E_T(k)$. Additionally, the evolution of the spectral shape of the turbulent cloud is visualised by plotting contours of $E(k, z, t)$ as exemplified in figure 2(c,d) for the same two experimental cases.

Figure 2(a) shows that mode k_3 and k_6 display the same variations in energy at all times, with both modes arriving at roughly the same time $\tau_3 U_0/L \approx \tau_6 U_0/L \approx 215$. This
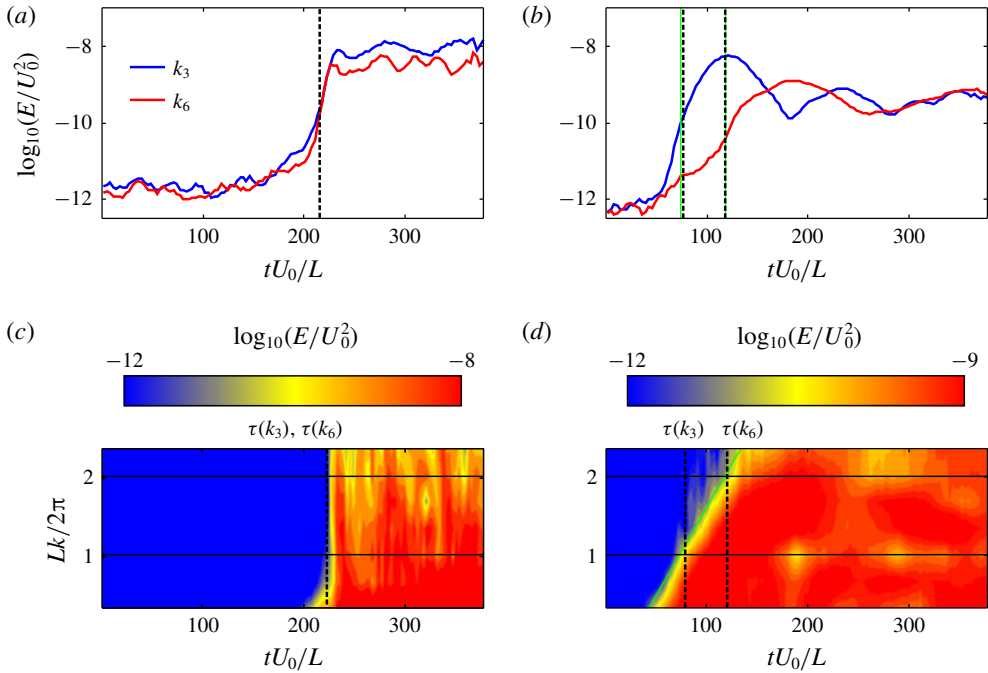
FIGURE 2. (*a,b*) Temporal energy profiles $E(k, t)$ for modes $k_3 L/2\pi \approx 1.0$ and $k_6 L/2\pi \approx 2.0$ at $Re_Q = 2500$ and a height $z/L = 4.91$. (*c,d*) Contour plots of $E(k, t)$, where solid black lines highlight $E(k, t)$ for modes k_3 and k_6. Experiments conducted at (*a,c*) $Ek = \infty$ and (*b,d*) $Ek = 4.25 \times 10^{-5}$. Arrival times ($\tau(k_3)$, $\tau(k_6)$) are represented by dashed lines. Green lines in (*b*) represent the theoretical arrival time for inertial waves of wavenumber k_3, k_6 respectively. Similarly, the green line in (*d*) represent the theoretical contour of linear inertial wave propagation across the entire spectrum.

is reflected in the near vertical contour in figure 2(*c*). Figure 2(*b*), however, shows that mode k_3 progresses substantially faster than mode k_6 arriving at time $\tau_3 U_0/L \approx 80$ and $\tau_6 U_0/L \approx 115$, respectively. This difference in displacement velocity observed in the rotating case translates into the slanted contour of figure 2(*d*).

3. Advection of the turbulent cloud with and without background rotation

3.1. *Non-rotating jet experiments*

We first analyse the motion of the turbulent front in the absence of a Coriolis force (i.e. $Ek = \infty$), where no propagative behaviour is expected, to enable us to quantify changes in behaviour when rotation is present. Under these circumstances the only available mechanism is advection. Figure 3 shows the motion of the front at $Re_Q = 6000$ for the first six modes of the Discrete Fourier Transform with wavenumber k_i, where $\{k_i\}_{i=1..6} = 2\pi i/(N\ell)$. Here N is the number of PIV grid points along the horizontal plane ($N = 64$) and $N\ell$ is this width of the resolved horizontal plane which is about 155 mm. For $Ek = \infty$ the motion of the turbulent front is independent of k. The position of the turbulent front follows a scaling of $(z - z_0)/L \approx (0.351 \pm 0.016)(\tau U_0/L)^{0.482 \pm 0.011}$ across all scales of the flow. This behaviour is observed for all Re_Q explored. Here, the offset z_0 is calculated so that
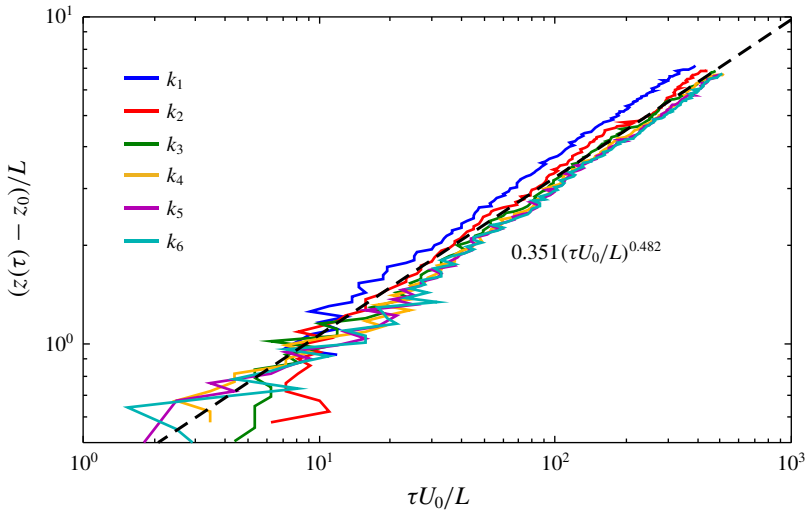
FIGURE 3. Arrival time τ at height z for the first six modes k_i at $Re_Q = 6000$ in the absence of rotation ($Ek = \infty$). The dashed line is a fit of the experimental data for $z \geqslant 0.8$.
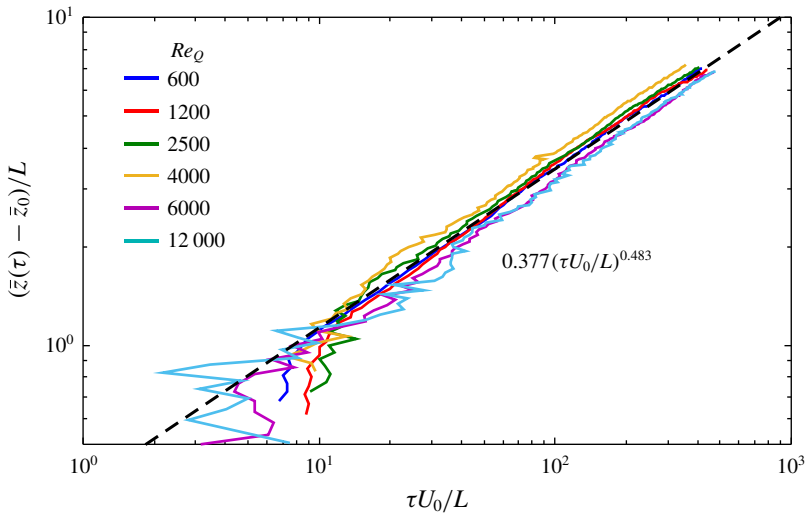

FIGURE 4. Arrival time τ at height z at $Ek = \infty$ across all Re_Q, where τ is taken as the average across first six modes k_i. The solid black line is a fit of data where $z/L \geqslant 0.8$.

the power law fit extends to $\tau = 0$. Since the jet is turbulent, and that all scales are displaced at the same velocity, the position of the turbulent front $\bar{z}(\tau)$ may be calculated as the average over the first six modes of the discrete Fourier transform used to calculate $E(k, z, t)$. Figure 4 shows the variations of $\bar{z}(\tau)$ with Re_Q in the absence of Coriolis force. By non-dimensionalising τ by the characteristic injection time L/U_0 the data for $\bar{z}$ collapse almost onto a single line for $\bar{z}/L \geqslant 0.8$. This shows that in the absence of rotation the non-dimensional arrival time is determined solely

by the injection velocity U_0 as

$$\frac{\bar{z}(\tau) - \bar{z}_0}{L} = (0.377 \pm 0.014) \times \left(\frac{\tau U_0}{L}\right)^{0.483 \pm 0.010}, \qquad (3.1)$$

with corresponding velocity of the turbulent front as it progresses in the quiescent fluid

$$\frac{U(z)}{U_0} = (6.41 \pm 0.11) \times 10^{-2} \left(\frac{z}{L}\right)^{-1.070 \pm 0.027}. \qquad (3.2)$$

The z^{-1}-profile closely resembles the axial velocity profile of a single steady turbulent jet (Pope 2000, p. 100), most likely because of the nature of our forcing. Nevertheless, the fact that the transient jet exhibits the same profile as the statistically steady jet, indicates that the jet develops in such a way that the flow behind the front is in a statistically steady state even though the front continues to progress. In other words, the front 'sweeps' through the quiescent fluid, leaving a statistically steady turbulent flow behind. This is confirmed by observing the shape of the turbulent region as seen figure 5(*a*). This region only evolves by extending upwards, as the front progresses, but not radially. This scenario is further supported as for the profile of a steady jet, momentum conservation implies that the turbulent region should grow linearly with the distance to the origin as a result. Figure 5(*a*) seems to confirm that the jet behind the turbulent front satisfies this property.

Scaling (3.1) is near identical to the front displacement law found experimentally by Dickinson & Long (1978) with an oscillating grid instead of jets. This law is itself in agreement with the theoretical prediction of Long (1978), expressed dimensionally as $z_{dim}(t) \sim K t_{dim}^{1/2}$, where constant K is expected to scale with the action generating the turbulence. While an exact determination of the parameters governing the variation of this quantity is not available in Dickinson & Long's (1978) grid experiments, $K \simeq (0.43 \pm 0.02)(U_0 L)^{1/2}$ in the present case of jet-driven turbulence. The displacement offset $\bar{z}_{0dim}$ lies in the range 0.5–2.0 cm, similar to the experiments of Dickinson & Long (1978) and Hopfinger & Toly (1976), most likely on the grounds that the small scale forcing from the grid and the jets lie in the same range of scales. Additionally, z_0 exhibits no variations of significance with either the wavelength considered or Re_Q (see figure 6, beyond fluctuations within the measurement error, which we estimate to approximately 0.5 cm). These results confirm that the 4-jet system generates a turbulent front with the same dynamics as the classic oscillating grid. Moreover they establish the scale independence of the advective front motion.

Physically, z_0 corresponds the virtual point from where turbulent advection starts. A possible reason for z_0 not to be zero is that the jet is not turbulent at $\tau = 0$: the first state of the development of the jet is laminar, followed by the development of instabilities, which in turn lead to turbulence in a finite time. Hence the initial advection may not follow the turbulent advection law. It follows that if the advected position of the turbulent front is extrapolated back to $\tau = 0$ according to that law, the result may not coincide with the bottom of the tank but with an offset position z_0.

3.2. *Advection in the presence of background rotation*

As mentioned in introduction, one of the main reasons for the choice the transient jet configuration is that momentum transport can easily be tracked through the displacement of the turbulent front. In order to differentiate advection from other momentum transport mechanisms in the rotating jet, we first need to understand how
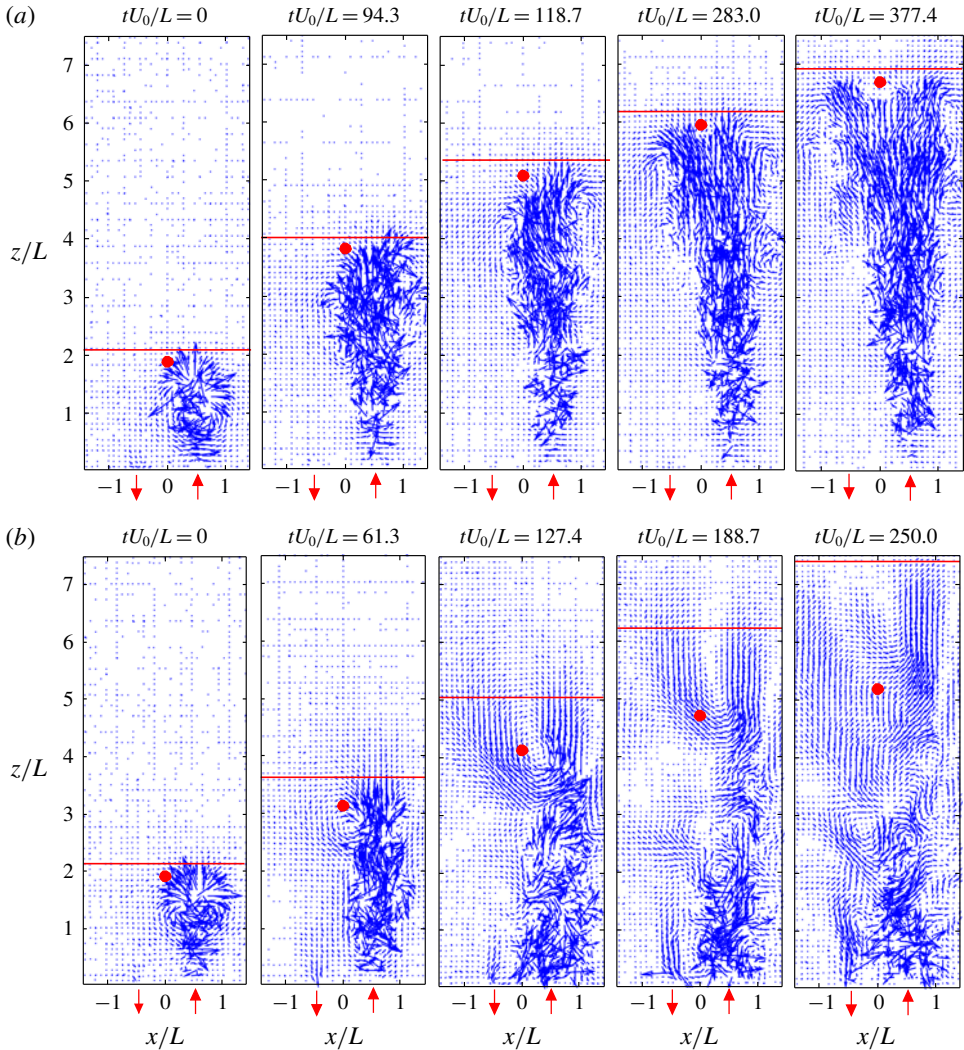
FIGURE 5. Snapshots of the jet velocity field for $Re_Q = 2500$ and (a) $Ek = \infty$ and (b) $Ek = 8.50 \times 10^{-5}$. The red dot shows the position $z^a(t)$ of a numerical particle initially positioned at $z_0/L = 2$, where $t = 0$ coincides $z/L = 2$. The red line shows the position of the front. The small difference in position between particle and front in (a) is artificial and caused by differences in sensitivity in the methods used to measure their position. Red arrows indicate the point of fluid injection/withdrawal. The supplementary movie (available at https://doi.org/10.1017/jfm.2019.1051) movie1.avi shows the simultaneous evolution of both jets represented here.

rotation affects advection itself. This is done by calculating the Lagrangian flow Φ associated with the two-dimensional flow field obtained from the PIV measurements for $\boldsymbol{u}(x, z, t)$. For a particle initially located at $\boldsymbol{r}_0 = (x(t=0), z(t=0)) = \boldsymbol{r}(t=0)$,

$$\boldsymbol{r}(t) = \Phi(\boldsymbol{r}_0, t) = \int_0^t \boldsymbol{u}(\boldsymbol{r}(t'), t') \, \mathrm{d}t'. \tag{3.3}$$
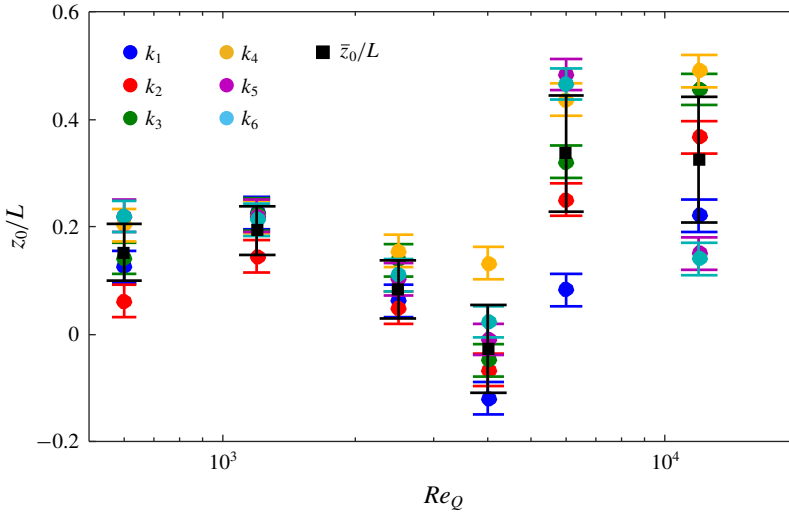
FIGURE 6. Offset z_0 measured across Re_Q and scales k_i at $Ek = \infty$.

For the purpose of determining the motion of the turbulent front, we shall consider advection of a particle in the z direction only and calculate its virtual motion if it were purely advected by the jet. Additionally, since we are interested in the movement of the front and not of an actual particle, we shall consider the maximum advection velocity across the x direction rather than the local one and define the purely advective displacement as

$$z^a(t) = \int_0^t \max_x \{\boldsymbol{u}(x, z^a(t'), t') \cdot \boldsymbol{e}_z\} \, \mathrm{d}t'. \tag{3.4}$$

It is noteworthy that the coordinate $z^a(t)$ does not track an actual fluid particle. Indeed, while fluid transport indeed occurs through advection, it does not occur through propagation of inertial waves. Momentum transport, on the other hand, does occur in both processes. More precisely, the turbulent front materialises the transport of the fluctuating part of the momentum. The evolution of $z^a(t)$ is represented in two ways: figure 7(a) shows $z^a(t)$ for $Re_Q = 1200$ and varying Ek, while 7(b) shows $z^a(t)$ for $Ek = 4.25 \times 10^{-5}$ and varying Re_Q. Here $t = 0$ is set to the time when the particle is first displaced from its initial location at $z^a(0)/L \approx 2$. Figure 5 show snapshots of the jet velocity field with and without rotation, with the position z^a represented by a single particle. In the absence of rotation the position of the particle closely follows that of the turbulent front i.e. $z^a(t) \approx z(t)$. When rotation is present, the advected particles initially follows the turbulent front but falls well behind after this initial phase. The beginning of this second phase, which can be identified in figure 7 as the point where the curves deviate from the $Ek = \infty$ case, coincides with the appearance of chevron patterns in the velocity field. These patterns are visible in figure 5 for $tU_0/L \geqslant 127.4$, and in the supplementary material (movie1.avi). They are a signature of inertial waves being emitted by the jets. A combination of frequency filtering and phase averaging (Cortet, Lamriben & Moisy 2010) revealed that the jets emit inertial wave packets of all possible frequencies $\omega < 2\Omega$ and propagation angles $\theta = \arccos(\boldsymbol{e}_k \cdot \boldsymbol{e}_z)$ corresponding to the dispersion relation of inertial waves (1.1a,b). The chevron patterns are a superposition of numerous waves, which allows
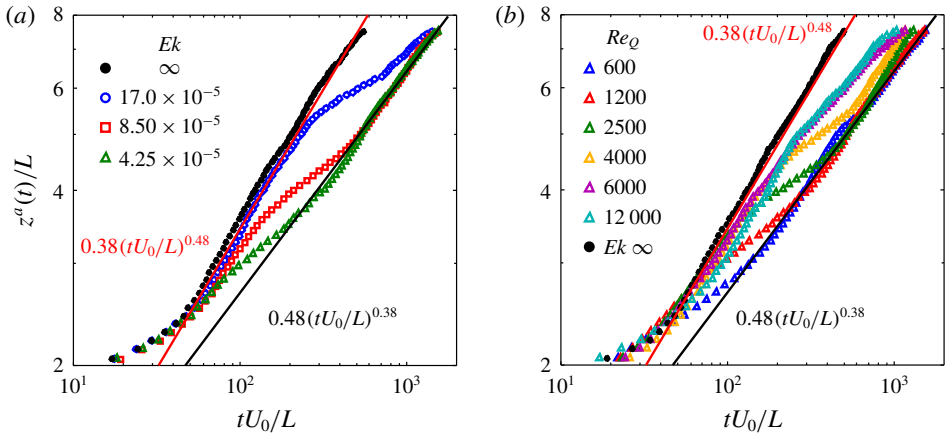
FIGURE 7. Position z^a of a particle initially placed at $z_0/L = 2$ as function of time. (a) $Re_Q = 1200$ with varying Ek. (b) $Ek = 4.25 \times 10^{-5}$ with varying Re_Q. Supplementary material movie2.avi contains a video showing the evolution of the jet next to the evolution of $z^a(t)$ and $z(t)$. Time $t = 0$ corresponds to the time when the particle is first displaced.

us to visualise the inertial waves. The details of this frequency analysis are reported in Brons *et al.* (2019).

The slowdown of advection can be understood in terms of momentum conservation: since part of the momentum is conveyed by inertial waves ahead of the 'purely advected' position, less momentum is locally available for purely advective momentum transport. The effect is all the more visible as rotation is important.

A third phase can be identified in figure 7 where the advection speeds up again, i.e. less momentum than in the previous phase is being transported by inertial waves. To understand why inertial waves suddenly lose their efficiency, we calculated the velocity U_R of a signal that would have been emitted at the onset of the jet, that would have travelled all the way up to the upper boundary of the vessel and back to the height z_R where the transition takes place, at the time it takes place t_R, i.e. $U_R = (2H - z_R - z_a(0))/t_R$. Figure 8(a) shows that U_R, normalised by the linear inertial wave velocity at scale L, $2\Omega L$, is nearly constant around 0.4 for all values of Ek, be it for a very small dependence on Re_Q, which may be attributed to weak nonlinearities (see figure 8b). Hence, the onset of the third phase coincides with the time at which inertial waves have reflected on the top wall and propagated back to the point of transition. This suggests that the loss of momentum transport may result from interferences between inertial waves propagating in opposite directions. Indeed, if an upward and a downward inertial wave interfere, the upward transport of angular momentum incurred as the upward wave progresses into the still fluid is partially cancelled by the downward momentum transport associated with the reflected wave. Interestingly, the wave velocity associated with the reflected wave is comparatively slower than the fastest upward propagating wave. The reason may be that momentum is not transported by a single wave but by a range of waves of different length scales and velocities. For the momentum transport to drop significantly, a sufficiently broad bandwidth of these waves must have reflected on the top wall, including slower waves, associated with smaller length scales.

On the subject of wave interactions, it is noteworthy that while interactions between incident waves and waves reflected on the walls of the vessels can sometimes be seen
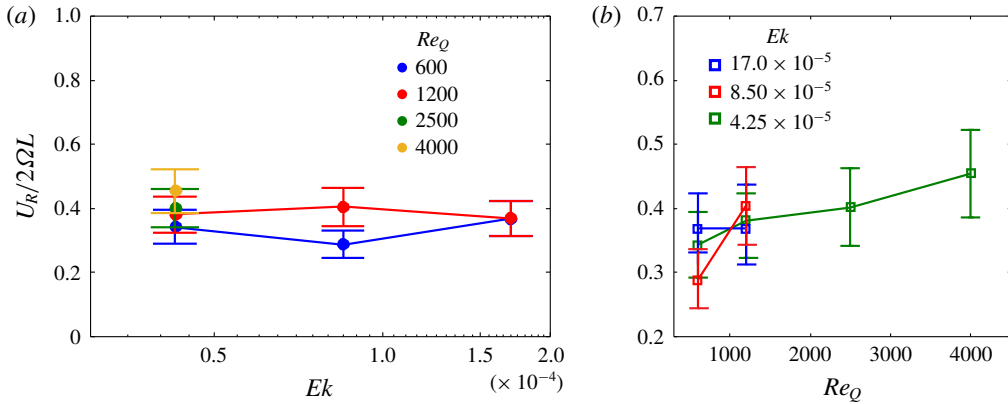
FIGURE 8. Reference velocity U_R based on the point of onset of the third advection phase normalised by the inertial wave velocity $2\Omega L$ versus (*a*) Ek and (*b*) Re_Q. Only experiments where the onset of third phase was observed were considered.

in the patterns, these are indicative of linear waves interference, and not of nonlinear wave interaction. As such, the intensity of the waves generated in our experimental set-up may be too low for inertial waves to enter the sort of nonlinear regime observed when intentionally focusing inertial waves in a region of interaction (Duran-Matute *et al.* 2013).

Following the suppression of momentum transport by inertial waves, the purely advected position resumes its progression at the non-rotating advective pace. Remarkably, not only is the velocity but also the position z^a independent of the rotation in this phase, as all positions follow a law:

$$\frac{z^a}{L} = (0.48 \pm 0.03) \left(\frac{tU_0}{L} \right)^{0.381 \pm 0.012}. \tag{3.5}$$

The value of the exponent, lower than the 0.5 value expected for pure advection may reflect that propagation by inertial waves is not entirely cancelled, as the reflected waves are less intense than the incident ones. Importantly, the dynamics observed in the second phase establishes that not only does rotation introduce an additional transport mechanism with inertial waves, but advection itself is suppressed as a result. Furthermore, the dynamics of the third phase suggests that momentum transport by inertial waves may not be efficient in confined flows, in particular quasi-two-dimensional ones, because waves reflecting on the boundaries.

4. Transition to inertial wave propagation

4.1. *Spectral profile of the turbulent front*

We now seek to characterise the motion of the actual turbulent front in cases where the experiment is rotating, having confirmed that it cannot be explained by advection alone. Figure 9 shows the spectral energy density contours of $E(k, z, t)$ at various heights z for $Re_Q = 1200$ across all values of Ek explored. This figure is representative of cases studied for all values of Re_Q. At $z/L = 0.94$ there is no discernible difference on the shape of contours between the cases with different values of Ek we investigated.
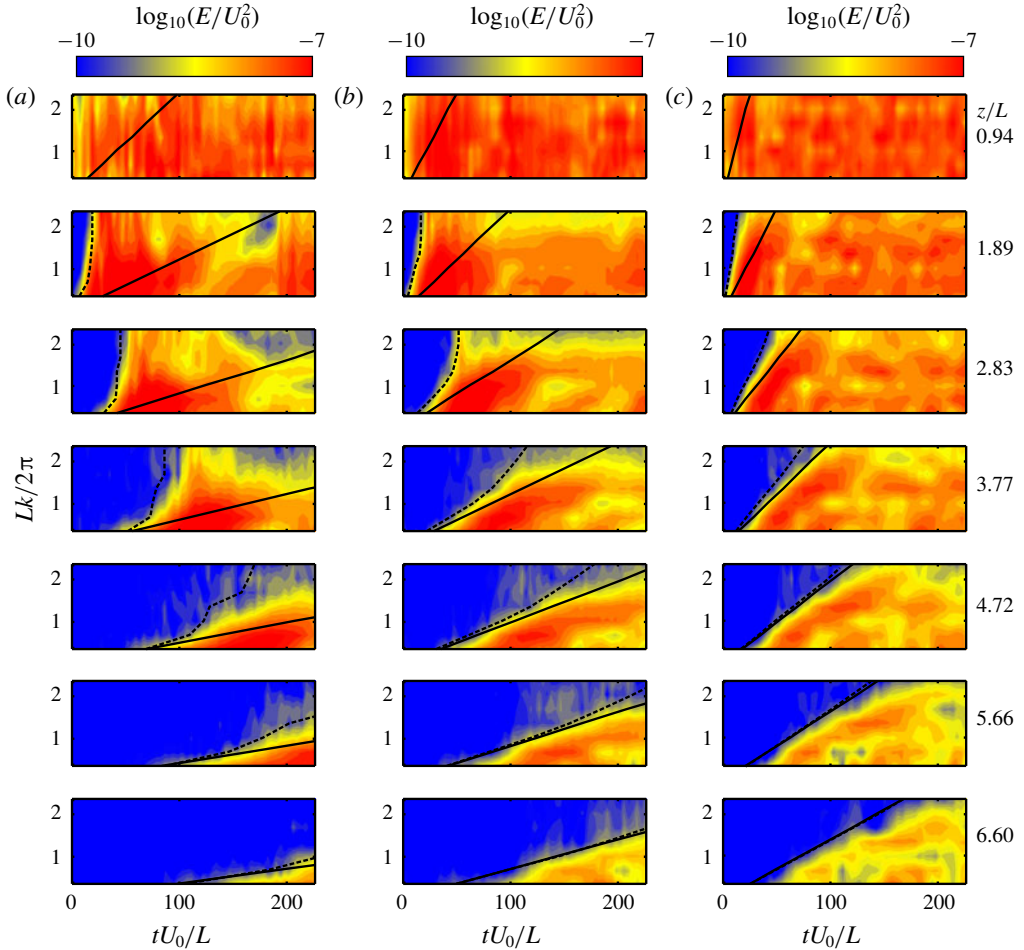
FIGURE 9. Contour plots of $E(k, t)$ across a number of heights z/L for $Re_Q = 1200$ at (a) $Ek = 17.0 \times 10^{-5}$, (b) $Ek = 8.50 \times 10^{-5}$ and (c) $Ek = 4.25 \times 10^{-5}$. The solid black line represents the shape of the energy contours assuming propagation is fully driven by inertial waves, i.e. $\tau = z/v_g(k)$. Dashed black lines represent the position of a numerical particle, based on (4.3).

Their near-vertical shape shows that all modes k arrive at the same time and thus all modes progress at approximately the same velocity.

For a given value of Ek, the spectral contour of the turbulent front progressively changes shape at greater distance z from the bottom wall, exhibiting three regions: the lower wavenumbers arrive at a time indicating that they progress at the group velocity of an inertial wave of the same wavenumber (marked by solid lines). At the higher wavenumbers, by contrast, the front continues to exhibit the flat profile that characterises advection by the jet. These two regions of the front are linked up by a rather narrow transition region. As z increases, the low-wavelength region occupies an increasingly large part of the spectrum, while the high-k advective region shrinks and eventually disappears in all cases we investigated. This is consistent with the morphology of the jet which spreads and therefore slows down away from the source,
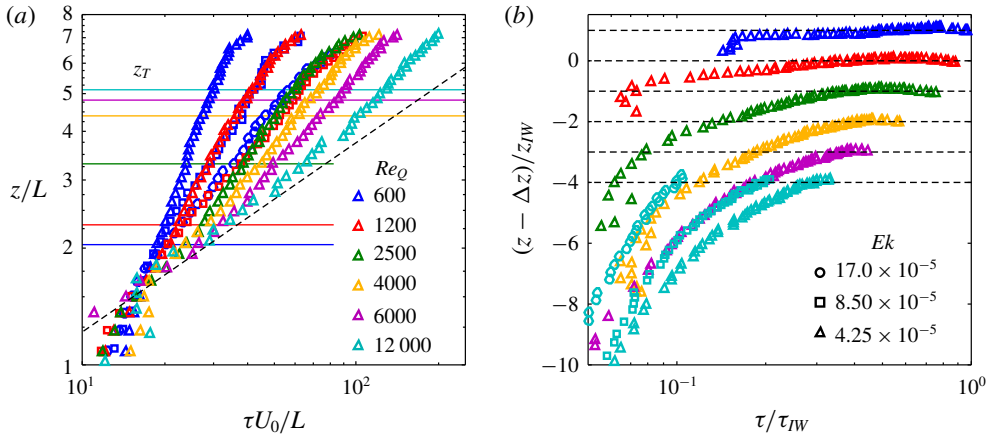
FIGURE 10. (a) Arrival time τ at height z for mode k_1 at $Ek = 4.25 \times 10^{-5}$ (triangles), $Ek = 8.50 \times 10^{-5}$ (squares) and $Ek = 1.70 \times 10^{-4}$ (circles). The dashed line represents (3.1). Coloured lines mark z_T where the motion of the turbulent front has transitioned to the propagative mechanism at $Ek = 4.25 \times 10^{-5}$. (b) z and τ normalised by propagation of inertial wave with wavenumber k_1, represented by the dashed lines. Position z is shifted by $\Delta z = z_{IW}(t) - z(t)$. Datasets have been further shifted down by a constant of 1 with respect to one another for clarity.

implying that advection progressively weakens as z increases. For higher rotation (lower values of Ek) pictured on the different columns of figure 9, the transition between the propagative and the advective parts of the front becomes increasingly sharp and displaces towards increasingly higher wavenumbers.

The overall picture is that structures of higher wavenumbers are advected by the jet whereas at low wavenumbers, larger structures propagate with inertial waves. As the Coriolis force that underpins inertial waves progressively overruns inertial forces associated with advection (either as z increases or as Ek decreases), low-wavenumber propagation invades an increasingly wider waveband at the expense of high-wavenumber advection.

4.2. *Transport of individual modes*

A finer perspective on the mechanism at play can be gained by tracking individual modes as they are transported along the jet. Considering individual modes offers the opportunity to compare their propagation to the group velocity of inertial waves of the same wavevector along their trajectory. Figure 10(a) shows such trajectories $z(t)$ for mode k_1, for several values of Re_Q at $Ek = 4.25 \times 10^{-5}$. The dashed line shows the trajectory of the turbulent front when $Ek = \infty$, i.e. driven by advection only. Trajectories at all Re_Q initially follow the advection trajectory and separate at a height which increases with Re_Q. Past this point, mode k_1 progresses faster than if it was advected.

To highlight regions of the trajectory that are governed by inertial waves propagation, the trajectories of mode k_1 are plotted in figure 10(b) for several values of Ek, using variables $(z - \Delta z)/z_{IW}$ and τ/τ_{IW}, where $z_{IW}(t) = 2\Omega t/k$, $z_{IW}(\tau_{IW}) = H$ and Δz is the offset between z and z_{IW}, measured near the top of the tank. In these new variables, displacements at the group velocity of mode k_1 follow horizontal lines.
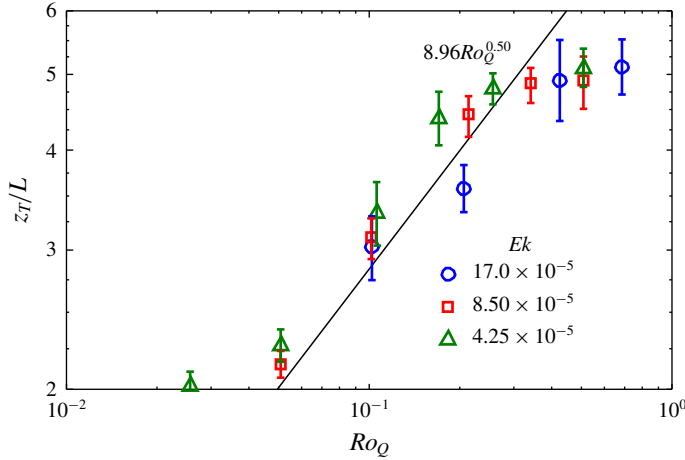
FIGURE 11. Height z_T beyond which the displacement of scales of wavenumber k_1 are driven by the propagative mechanism.

As expected, trajectories start away from the horizontal propagation lines in the initial advective phase identified in figure 10(a), but gradually bend toward them to end up following them closely. This shows that inertial wave propagation eventually takes over advection. For $Re_Q = 12\,000$ and $Ek = 17.0 \times 10^{-5}$ trajectories barely meet the theoretical propagation line, indicating that propagation never fully takes over within our experimentally accessible parameters. Overall convergence is all the faster as Re_Q and Ek are low, as inertial forces delay the transition from advection to propagation, while rotation accelerates it.

To quantify the transition from the advective to the propagative mechanism, we define the point of transition as $z_T = |z/(z_{IW} + \Delta z) - 1| \leqslant \beta$, where β is a chosen threshold value. The value of β has to be chosen as low as possible; however, as β is lowered, the results become increasingly susceptible to experimental noise. To keep noise to a low level, we chose $\beta = 0.2$ and verified that the results were independent of the exact value we chose. Figure 11 shows z_T for k_1 across all Re_Q and Ek explored, with the exception of those where the transition was not fully achieved (such as for $Re_Q = 12\,000$ and $Ek = 17.0 \times 10^{-5}$). Values of z_T mostly obey a scaling dependent on the Rossby number only:

$$z_T/L \simeq (8.96 \pm 0.74) Ro_Q^{1/2}. \tag{4.1}$$

A few points depart from this law for $Ro_Q > 3 \times 10^{-1}$. We could verify that this behaviour is an artefact of the method used to determine z_T, as lowering the value of β shifts this point to higher values of Ro_Q and z_T/L. Scaling (4.1) can be understood by considering that at the transition between the two phases, the length of the jet z_T has reached a point where Coriolis forces are sufficient to balance inertia. Considering z_T as the largest length scale, in dimensional terms, it must satisfy $U(z_T)/z_T \sim 2\Omega$. In the absence of rotation effects, the jet develops as $U(z)/U_0 \sim d/z$ (Pope 2000, p. 100), so z_T must scale as $z_T \sim (U_0 d/2\Omega)^{1/2}$, or equivalently, $z_T/L \sim Ro_Q^{1/2}$, as in (4.1). A similar criterion was put forward by Burmann & Noir (2018) to explain the breakdown of inertial wave propagation in a spun up cylinder where the waves were emitted by a topography of the bottom wall. When turbulence is forced by

an oscillating grid, Dickinson & Long (1983) similarly observe that the progression of the front is not affected by rotation in the early stages up to a critical distance, which these authors express (in our notations) as $z_T \simeq 0.36(f S^2/\Omega)^{1/2}$, in terms of the frequency f and stroke S of the grid. As such, $f S$ is equivalent to forcing velocity U_0 and the scaling for z_T associated with the oscillating grid can be rewritten $z_T/S \simeq 0.36 Ro_Q^{1/2}$. It is similar to (4.1), even though reference length scales S and L are not necessarily directly comparable and the upward motion imprinted by the jet may contribute to stretch the patch upwards. It is noteworthy that the transition point for mode k_1 coincides with the transition point for the whole front. Indeed, wavenumber k_1 corresponds to the largest length scale, with the fastest inertial wave within the set of wavelengths captured within the visualisation area. The fact that no inertial wave travels faster than that of scale k_1 confirms that $W \simeq 3L$ captures the largest scales of the turbulent patch. As such the visualisation area we chose is suitable to capture the propagative processes responsible for momentum transport. For the same reason, the point z_T also corresponds to the point of transition where advection itself starts being suppressed by the effects of rotation (see § 3).

4.3. *Scaling for the transition between advection and propagation*

The example of k_1 illustrates that fluctuations are first advected in the low part of the jet, as advection dominates near the injection point. As they progress through the fluid domain, advection subsides as the jet spreads. At the same time, the mean centreline velocity decreases and propagation by inertial waves takes over as the main transport mechanism. The last step is to understand how this mechanism expresses at other wavelengths $k > k_1$. To this end, we first note from figures 10 and 11 that all curves for the displacement of fluctuations of wavenumber k_1 gradually transition away from the pure advection trajectory and converge to the propagative trajectory at $z = z_T$. At this point their displacement velocity matches to the propagation velocity of linear inertial waves. Expressing this property for fluctuations of wavelength k yields the condition (here dimensionally written)

$$U(z) \simeq V_g(k) = \frac{2\Omega}{k}. \tag{4.2}$$

In other words, the transition from advection to propagation for fluctuations of wavelength k takes place when the local, scale-dependent Rossby number $Ro(k, z) = kU(z)/2\Omega$ reaches unity. Another way to express this is that fluctuations are advected at the fastest of the local advection velocity and the group velocity of inertial waves.

To test this criterion on the entire spectrum, we calculate the arrival time of fluctuations for $k \in [0, 40]$, for the values of z displayed on figure 9, using the modified expression of the Lagrangian flow:

$$z(k, t) = \int_0^t \max\{\max_x\{\boldsymbol{u}(x, z(t'), t') \cdot \boldsymbol{e}_z\}, v_g(k)\}\, dt'. \tag{4.3}$$

From this expression, we extract the arrival time $\tau(z, k)$ of fluctuations with wavenumber k at height z, which forms the spectral shape of the turbulent front. The results are reported on figure 9, which is representative of all other values of Re_Q we considered. In all cases, the motion of a numerical particle subject to (4.3) matches the actual contours of $E(k, z, t)$ closely for $z/L \geqslant 1.5$. It indeed captures all

three regions identified in §4.1. This indicates in particular, that in the intermediate region, the arrival time results from an initial advective phase of comparable duration to a second propagative phase, so that the arrival time falls somewhere between a pure advective and a pure propagative time.

5. Conclusion and discussion

We have analysed the scale-by-scale transport mechanisms in rotating turbulence. The results were obtained by examining the motion of the turbulent front generated during the transient flow of four jets penetrating into or extracted from a rotating vessel of quiescent fluid, and directed along the axis of rotation. In the absence of rotation, the distance from the jet source covered by disturbances evolves (in dimensional variables) as $(z(t) - z_0)/L \simeq 0.377(U_0 t/L)^{0.483}$ (U_0 and L are the jet inlet velocity and the distance between the jets, respectively). This law is in good agreement with Long's (1978) law for the global displacement of a turbulent front, with an offset $z_0 \simeq 0.5$–2.0 cm, incidentally consistent with the values experimentally found by Dickinson & Long (1978) in experiments with an oscillating grid. Additionally, we established that this law is valid at all scales, regardless of their transversal wavenumber k, and of the Reynolds number based on the inlet jet velocity Re_Q. In the presence of rotation, the turbulent front is advected exactly as in the non-rotating case up to a distance $z_T/L \simeq 8.96 Ro_Q^{1/2}$, where the Coriolis force becomes larger than inertia. Past this point, the development of the jet is dominated by the faster propagation of inertial waves. However, since momentum is redistributed over a larger volume by inertial waves, it is locally weaker. As a consequence, advection itself is suppressed by rotation.

In the last phase of the jet's evolution, inertial waves reflected on the vessel's wall of the fluid vessel interfered with inertial waves travelling up, resulting in a suppression of the total transport by inertial waves. This suggests that in confined flows, inertial waves may not be able to transport momentum efficiently. This is particularly relevant in the quasi-two-dimensional limit, where our recent experiments showed that they were indeed not driving the dynamics (Brons *et al.* 2019).

The scale-by-scale analysis of the propagation enabled us to answer the questions set out in the introduction:

(i) A clear separation exists between scales advected by inertial waves and by the local mean flow.

(ii) The border between the two regimes is set by the Rossby number based on the transversal wavelength of the scale considered and the local large scale velocity as $Ro_k(k, \boldsymbol{x}) = kU(\boldsymbol{x})/2\Omega = 1$. In that sense, this criterion is local both in space, time and scale.

The implication of this phenomenology is that the transport of turbulent fluctuations as turbulence progresses into the quiescent fluid follows two phases: one purely controlled by local advection for $Ro_k(k, z) > 1$ and one purely controlled by the propagation of inertial waves for $Ro_k(k, z) < 1$. The spectral locality of the transition complements the recent evidence for its spatial locality found by McDermott & Davidson (2019).

In other turbulent flows with more complex flow topology, the same phenomenology would imply that structures may be alternately convected by larger structures and propagated by inertial waves. However, it is worth pointing out that the fact that advection dominates at a given scale does not mean that inertial waves do not

exist at that scale. Just like the transversal sweeping of inertial waves in nearly two-dimensional flows (Campagne *et al.* 2015). Axial advection of inertial waves could take place in our set-up, but would be shadowed if advection was the fastest mechanism. More generally, our result does not exclude the possibility that inertial waves at small scales may be axially or laterally convected by faster advection too. These remarks apply in particular to non-transient turbulent flows. Indeed, an important feature of the transient problem studied in this paper is the fact that inertial waves are emitted by random fluctuations in a turbulent region where rotation does not dominate. A similar phenomenology may exist in turbulent flows, even when the macroscopic Rossby number remains well below unity, provided random fluctuations also exist at a sufficiently small scale to escape the influence of rotation. Such fluctuations may act as random sources of inertial waves competing with local advection to transport momentum. Unlike in transient problems where the displacement of the turbulent front offers a convenient way to track momentum transport, however, the two mechanisms are more difficult to disentangle in statistically steady turbulence, especially if unlike for the jet, momentum is not advected in a preferred direction.

Finally, while the mechanisms found here do not exclude the possibility that nonlinear interactions may participate in the build-up of large quasi-two-dimensional structures, they illustrate that linear inertial waves govern transport mechanisms at the large scales, as shown by Davidson *et al.* (2006), but they also dominate down to the level of smaller scales as long as the local balance of Coriolis force and advection favours the former. More generally, it is not unusual that turbulence dynamics be controlled at the scale level by linear processes, as illustrated in magnetohydrodynamic turbulence at low magnetic Reynolds number, where the anisotropy of individual scales is controlled by the balance between inertia and momentum diffusion by the Lorentz force (Sommeria & Moreau 1982; Pothérat & Klein 2014; Baker *et al.* 2018). Having said this, linear waves themselves can also interact nonlinearly and lead to turbulence when they are sufficiently energised, as demonstrated with inertial waves by Duran-Matute *et al.* (2013).

Acknowledgements

Supplementary movies

Supplementary movies are available at https://doi.org/10.1017/jfm.2019.1051.

REFERENCES

BAKER, N., POTHÉRAT, A., DAVOUST, L. & DEBRAY, F. 2018 Inverse and direct energy cascades in three-dimensional magnetohydrodynamic turbulence at low magnetic Reynolds number. *Phys. Rev. Lett.* **120**, 224502.

BARTELLO, P., MÉTAIS, O. & LESIEUR, M. 1994 Coherent structures in rotating three-dimensional turbulence. *J. Fluid Mech.* **273**, 1–29.

BRONS, J. A., THOMAS, P. J. & POTHÉRAT, A. 2019 Mean flow anisotropy without waves in rotating turbulence. arXiv:1902.07984.

BURMANN, F. & NOIR, J. 2018 Effects of bottom topography on the spin-up in a cylinder. *Phys. Fluids* **30** (10), 106601.

CAMBON, C., MANSOUR, N. N. & GODEFERD, F. S. 1997 Energy transfer in rotating turbulence. *J. Fluid Mech.* **337**, 303–332.

CAMBON, C. & SCOTT, J. F. 1999 Linear and non-linear models in anisotropic turbulence. *Annu. Rev. Fluid Mech.* **31**, 1–53.

CAMPAGNE, A., GALLET, B., MOISY, F. & CORTET, P. P. 2015 Disentangling inertial waves from eddy turbulence in a forced rotating-turbulence experiment. *Phys. Rev.* E **91**, 043016.

CAMPAGNE, A., GALLET, B., MOISY, F. & CORTET, P. P. 2014 Direct and inverse energy cascades in a forced rotating turbulence experiment. *Phys. Fluids* **26**, 125112.

CORTET, P. P., LAMRIBEN, C. & MOISY, F. 2010 Viscous spreading of an inertial wave beam in a rotating fluid. *Phys. Fluids* **22**, 086603.

DAVIDSON, P. A. 2013 *Turbulence in Rotating, Stratified and Electrically Conducting Fluids*. Cambridge University Press.

DAVIDSON, P. A. 2015 *Turbulence: An Introduction for Scientists and Engineers*. Oxford University Press.

DAVIDSON, P. A., STAPLEHURST, P. J. & DALZIEL, B. 2006 On the evolution of eddies in a rapidly rotating system. *J. Fluid Mech.* **557**, 135–144.

DICKINSON, S. C. & LONG, R. R. 1983 Oscillating-grid turbulence including effects of rotation. *J. Fluid Mech.* **126**, 315–333.

DICKINSON, S. C. & LONG, R. R. 1978 Laboratory study of the growth of a turbulent layer of fluid. *Phys. Fluids* **21** (10), 1698–1701.

DURAN-MATUTE, M., FLÒR, J.-B., GODEFERD, F. S. & JAUSE-LABERT, C. 2013 Turbulence and columnar vortex formation through inertial-wave focusing. *Phys. Rev.* E **87**, 041001.

GALLET, B. 2015 Exact two-dimensionalization of rapidly rotating large-Reynolds-number flows. *J. Fluid Mech.* **783**, 412–447.

GREENSPAN, H. P. 1968 *The Theory of Rotating Fluids*. Cambridge University Press.

HOPFINGER, E. J., BROWAND, F. K. & GAGNE, Y. 1982 Turbulence and waves in a rotating tank. *J. Fluid Mech.* **125**, 505–534.

HOPFINGER, E. J. & TOLY, J.-A. 1976 Spatially decaying turbulence and its relation to mixing across density interfaces. *J. Fluid Mech.* **78** (1), 155–175.

KOLVIN, I., COHEN, K., VARDI, K. & SHARON, E. 2009 Energy transfer by inertial waves during the buildup of turbulence in a rotating system. *Phys. Rev.* **102**, 014503.

LONG, R. R. 1978 Theory of turbulence in a homogeneous fluid induced by an oscillating grid. *Phys. Fluids* **21** (10), 1887–1888.

MCDERMOTT, B. R. & DAVIDSON, P. A. 2019 A conjecture for the dipolar-multipolar dynamo transition. *J. Fluid Mech.* **874**, 995–1020.

MCEWANS, A. D. 1976 Angular momentum diffusion and the formation of cyclones. *Nature* **260**, 126–128.

MOORE, D. W. & SAFFMAN, P. G. 1969 The flow induced by the transverse motion of a thin disk in its own plane through a contained rapidly rotating viscous liquid. *J. Fluid Mech.* **39** (4), 831–847.

MOORE, D. W. & SAFFMAN, P. G. 1968 The rise of a body through a rotating fluid in a container of finite length. *J. Fluid Mech.* **31** (4), 635–642.

PEDLOSKY, J. 1987 *Geophysical Fluid Dynamics*. Springer.

POPE, S. B. 2000 *Turbulent Flows*. Cambridge University Press.

POTHÉRAT, A. 2012 Three-dimensionality in quasi-two dimensional flows: recirculations and Barrel effects. *Europhys. Lett.* **98**, 64003.

POTHÉRAT, A. & KLEIN, R. 2014 Why, how and when MHD turbulence at low Rm becomes three-dimensional. *J. Fluid Mech.* **761**, 168–205.

SMITH, L. M. & WALEFFE, F. 1999 Transfer of energy to two-dimensional large scales in forced, rotating three-dimensional turbulence. *Phys. Fluids* **11**, 1608–1622.

SOMMERIA, J. & MOREAU, R. 1982 Why, how and when MHD turbulence becomes two-dimensional. *J. Fluid Mech.* **118**, 507–518.

STAPLEHURST, P. J., DAVIDSON, P. A. & DALZIEL, B. 2008 Structure formation in homogeneous freely decaying rotating turbulence. *J. Fluid Mech.* **598**, 81–105.

TAYLOR, G. I. 1922 The motion of a sphere in a rotating liquid. *R. Soc. Lond.* A **102**, 180–189.

THIELICKE, W. & STAMHUIS, E. J. 2014 PIVlab towards user-friendly, affordable and accurate digital particle image velocimetry in matlab. *J. Open Res. Softw.* **2** (1), e30.

THOMSON, J. 1868 *Letter to Lord Kelvin (W. Thomson)*. Glasgow University Library.

VANYO, J. P. 1993 *Rotating Fluids in Engineering Science*. Dover Publications.

YAROM, E. & SHARON, E. 2014 Experimental observation of steady inertial wave turbulence in deep rotating flows. *Nat. Phys.* **10** (7), 510–514.